

Dust Rings and Cavities in the Protoplanetary Disks around HD 163296 and DoAr 44

HARRISON LEIENDECKER,^{1,2} HANNAH JANG-CONDELL,^{1,3} NEAL TURNER,² AND ADAM D. MYERS¹

¹*University of Wyoming, 1000 E. University, Dept 3905, Laramie, WY 82071*

²*Jet Propulsion Laboratory, California Institute of Technology, 4800 Oak Grove Drive, Pasadena, CA 91109*

³*NASA Headquarters, 300 Hidden Figures Way, Washington, DC 20546*

ABSTRACT

We model substructure in the protoplanetary disks around DoAr 44 and HD 163296 in order to better understand the conditions under which planets may form. We match archival millimeter-wavelength thermal emission against models of the disks' structure that are in radiation balance with the starlight heating and in vertical hydrostatic equilibrium, and then compare to archival polarized scattered near-infrared images of the disks. The millimeter emission arises in the interior, while the scattered near-infrared radiation probes the disks' outer layers. Our best model of the HD 163296 disk has dust masses $81 \pm 13 M_{\oplus}$ in the inner ring at 68 au and $82^{+26}_{-16} M_{\oplus}$ in the outer ring at 102 au, both falling within the range of estimates from previous studies. Our DoAr 44 model has total dust mass $84^{+7.0}_{-3.5} M_{\oplus}$. Unlike HD 163296, DoAr 44 as of yet has no detected planets. If the central cavity in the DoAr 44 disk is caused by a planet, the planet's mass must be at least $0.5 M_J$ and is unlikely to be greater than $1.6 M_J$. We demonstrate that the DoAr 44 disk's structure with a bright ring offset within a fainter skirt can be formed by dust particles drifting through a plausible distribution of gas.

1. INTRODUCTION

Observations across a wide range of wavelengths have provided detailed information on the variety of substructures in protoplanetary disks (ALMA Partnership et al. 2015; Monnier et al. 2017; Andrews et al. 2018; Avenhaus et al. 2018). The frequency at which these substructures are observed indicates they are likely a near-ubiquitous feature of disk evolution (van der Marel et al. 2019). Possible causes of these substructures include fluid dynamic interactions (Heinemann & Papaloizou 2009; Flock et al. 2011), condensation fronts with or without pressure bumps (Gonzalez et al. 2017; Stammer et al. 2017), and dynamical interactions of the disk with planetary companions (Duffell 2020). Rings, gaps, and cavities in particular are most simply explained using a young protoplanet, though protoplanets are directly detected in just a few cases (Sallum et al. 2015; Kepler et al. 2018; Zhou et al. 2022).

The density and temperature distributions within the parent disk set the conditions for planet formation. The surface density of the gas reflects the speed at which angular momentum is transported in the disk (Hartmann et al. 1998) and determines how forming planets' orbits evolve (Baruteau et al. 2014). Interactions between the disk's gas and solid particles affect the particles' growth, drift, and mutual collisions (Birnstiel et al. 2012). The temperatures at different locations govern basic prop-

erties including the gas scale height and the speeds at which disturbances propagate through the gas. Beyond the inner disk, the transfer of stellar irradiation from grains in the upper layer of the disk to the midplane primarily determines the temperature structure (Kenyon & Hartmann 1987; Chiang & Goldreich 1997). Even sub-Jovian-mass planets can alter the distribution of gas in the disk nearby, which in turn affects the planets' growth (Jang-Condell & Sasselov 2003; Guilera et al. 2019).

For this investigation, we carry out calculations with a radiative transfer code (Jang-Condell 2008) to recreate observations at multiple wavelengths of disks around two stars: HD 163296 and DoAr 44. Hydrostatic disk models in radiative equilibrium with the starlight are constructed to replicate ALMA observations of thermal emission (Andrews et al. 2018; Cieza et al. 2021). We also compare synthetic polarized scattered near-infrared images of the best-fit models to observations from GPI and VLT-SPHERE (Monnier et al. 2017; Avenhaus et al. 2018).

We select the disk around the Herbig Ae star HD 163296 because it is a well studied target (Andrews et al. 2018; Isella et al. 2018; Pinte et al. 2018). This gives us a good baseline against which to validate our model results. The star is located 101.5 pc from the Sun (Gaia Collaboration et al. 2018), and the disk has mass estimates as large as $0.2 M_{\odot}$ (Muro-Arena et al. 2018). There are two prominent rings in the thermal

emission beyond an inner disk, but only the inner ring is observed in polarized scattered light (Figure 1). The clear ring structure has made HD 163296 one of the best examples of disks thought to be shaped by protoplanets. Kinematic deviations observed in CO channel maps of the disk near 94 au (Izquierdo et al. 2021) and 260 au (Pinte et al. 2018) are well explained by planets at those radii.

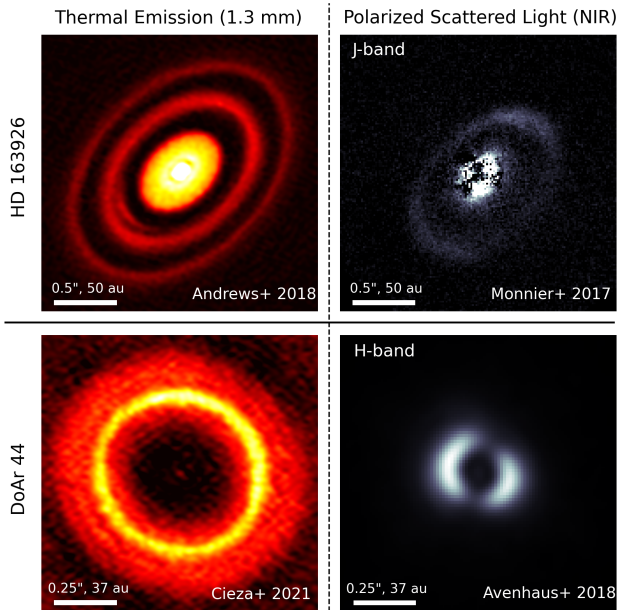


Figure 1. Observations of HD 163296 (top) and DoAr 44 (bottom). Thermal emission images (1.3 mm) are shown on the left with a red scale and polarized scattered light images (J-band and H-band) are both shown on the right with a blue scale. Both of the thermal emission data were taken with ALMA (Andrews et al. 2018; Cieza et al. 2021). The J-band data for HD 163296 are from Gemini Planet Imager (Monnier et al. 2017). The H-band data for DoAr 44 are from SPHERE (Avenhaus et al. 2018). The two disks demonstrate some of the variety of appearances ring-like substructure may have in disks.

We model the disk around the T-Tauri star DoAr 44 (also known as ROXs 44, WSB 72, or HBC 268) because it is a less studied disk with an interesting morphology. DoAr 44 is 146.3 pc from the Sun (Gaia Collaboration et al. 2018). The disk has a peculiar “ring-within-a-ring” or “ring-skirt” morphology observed in thermal emission with ALMA (Figure 1). The ring surrounds a central cavity. The disk has also been observed in H-band polarized light (Avenhaus et al. 2018). At this NIR wavelength, the ring of scattered light appears to be inside the radius of the cavity observed in thermal emission. Two breaks nearly opposite each other in the scattered-light ring suggest shadowing by a highly-inclined inner

disk (Casassus et al. 2018). The SED has an excess at $\lambda \leq 4.5 \mu\text{m}$ from an inner disk and a faint mid-IR flux, making this a pre-transition disk according to Cieza et al. (2021).

The paper is laid out as follows. A description of our radiative transfer models and methods is given in Section 2. Results for the surface densities and temperatures of the two disks are in Section 3, and a discussion of these results and their implications for potential planets is provided in Sections 4–7. Specifically, in Section 4 we compare our dust mass estimate for HD 163296 and DoAr 44 to previous results. We discuss potential embedded planets in the disks in Section 5, as well as additional considerations for the unusual morphology of DoAr 44 in Section 6. A discussion of our scattered light results is provided in Section 7. Finally, in Section 8 we summarize the study and suggest further directions for investigation.

2. METHODS

2.1. Observations

The observations of HD 163296 we use are from the Atacama Large Millimeter/submillimeter Array (ALMA) (Andrews et al. 2018) and Gemini Planet Imager (GPI) (Monnier et al. 2017). The ALMA data were taken as part of the DSHARP project in September of 2017 in Band 6 around 1.3 mm (Isella et al. 2018). The GPI data were taken in April of 2014, showing polarized scattered light in the J-band. The observations of DoAr 44 were taken with ALMA (Cieza et al. 2021) and VLT SPHERE (Avenhaus et al. 2018). These ALMA data were taken in Band 6 as part of the ODISEA survey. The SPHERE (Spectro-Polarimetric High-contrast Exoplanet REsearch) data were taken in the H-band as part of the DARTTS-S survey.

2.2. Radiative Transfer Modeling

We use a radiative transfer code (hereafter JC2008) from Jang-Condell (2008). The code calculates temperature and density profiles of the two disks and then creates synthetic observations of their thermal emission and polarized scattered light. The approach is based on the techniques developed by Calvet et al. (1991) and D’Alessio et al. (1998) for modeling plane-parallel disks in one spatial dimension.

The JC2008 code solves for the variation with optical depth τ of the radiation intensity and the temperature, under the assumption that radiative heating balances radiative cooling. The code includes both scattering and absorption of stellar irradiation and thermal emission throughout the disk. The code applies the Eddington approximation and the Milne-Strittmatter treatment to

the optical radiation from the star incident on the disk at angle $\cos^{-1} \mu$, and also to the disk’s re-radiated thermal infrared emission. Under the Milne-Strittmatter treatment, the radiative transfer calculation splits the radiation into two components: the light from the star and the thermal emission from the disk. The opacities for the thermal disk temperatures are calculated for a disk temperature of 100 K.

The opacities used are as follows: the Rosseland mean opacity for the disks’ thermal emission (χ_R), the Planck mean opacity integrated over the disks’ spectra (κ_P), and the Planck mean opacities integrated over the stellar spectra for absorption alone (κ_P^*) and for absorption plus scattering (χ_P^*). The single scattering albedo is $\sigma = 1 - \kappa_P^*/\chi_P^*$. The values for the opacities of the disks are provided in Section 2.3 (Table 1).

The JC2008 code extends the techniques from Calvet et al. (1991) and D’Alessio et al. (1998) to general, curved, three-dimensional surface. The code divides the surface of the model disk into patches, each of which can be approximated as locally plane-parallel, but with its own orientation relative to the incident radiation. Furthermore, having determined the temperatures, the code updates the density distribution to restore vertical hydrostatic equilibrium, then iterates between temperature and density updates until the structure approaches joint radiative and hydrostatic balance. Complete details of the JC2008 code are in Jang-Condell (2008).

To create our disk models, we begin with the temperature structure from an unperturbed disk. Since the observed rings have roughly-Gaussian surface brightness profiles, we form the model disk’s surface density profile by summing Gaussians. We use JC2008 to compute the temperature profile based on the new density profile. Then we iterate between updating the temperature and restoring vertical hydrostatic equilibrium by integrating the equation of vertical force balance, keeping temperature a fixed function of column depth.

We construct synthetic thermal emission and scattered-light observations by solving the transfer equation on a grid of rays extending from the disk towards the observer, enabling comparison of the models against the ALMA and GPI or SPHERE data. Unlike the iterative calculation of the disk’s structure, this calculation uses the specific opacities at the designated wavelengths of the synthetic observations instead of the mean opacities. Both absorption and scattering are considered for the image generation of the thermal emission and scattered light. The method of image construction is fully described in Jang-Condell (2009). Finally, we find a best fit to the thermal emission data by searching the

parameter space whose axes are the rings’ radial locations, peak dust surface densities, and widths.

2.3. Disk and Stellar Model Parameters

The simulation boxes of the models were set in cylindrical coordinates. The radial grid has 256 elements for each disk model to cover strictly the regions of observed ring structure. The height extends from the mid-plane to h_{box} with 128 grid elements, where h_{box} is twice the height of the surface of the unperturbed disk at the model center. The surface of the disk is defined to be at an optical depth of $\tau_s = 2/3$ for stellar radiation along the line of sight. Finally, the radiative transfer code assumes that the disk is axisymmetric with 32 grid elements spanning an angle $\theta = \pi/3$. Processing power is the main constraint in the choice of our overall grid size.

Fixed input parameters for the HD 163296 and DoAr 44 models are listed in Table 1. The stellar parameters (M_* , R_* , and T_{eff}) were taken from previous studies (listed in the table references). We determined the inclination and position angle of the disks independently by fitting ellipses to the rings in the ALMA observations with the Python package `emcee` (Foreman-Mackey et al. 2013). We assume that the ellipses are circular rings viewed from an inclination. The ellipses were fit with five free parameters: semimajor axis (a), eccentricity (e), position angle (PA), x_0 , and y_0 . The goodness of fit was determined using the ALMA data by maximizing surface brightness along the ellipse. Inclinations were calculated from the eccentricities assuming that the rings are circularly symmetric, and the semimajor axes provided the initial value for the rings’ radius as part of our grid-based search of ring parameters.

Viscosity ν and stellar accretion \dot{M}_* do not explicitly play a role in this radiative transfer code. In the formulation of the JC2008 code, both ν and \dot{M}_* determine the initial surface density. Our method instead turns the surface density into a free parameter that is varied to find the best fit. Furthermore, the flux from accretion heating scales as $F_{\text{acc}} \propto r^{-3}$ at larger radii (Pringle 1981). Even for the largest plausible values for accretion rate and optical depth, the accretion heating in our constant α disk model becomes negligible beyond 10 au compared to the heating from stellar flux, which scales as $F_{\text{irr}} \propto r^{-2}$ (D’Alessio et al. 2001).

2.4. Rings and Gap Shapes: Gaussian Rings

Initially, we formed gaps in the disk using gap shapes from Duffell (2020). This gap formulation is empirically derived from hydrodynamic simulations, and therefore is better suited to fit gaps in the gas distribution than the coarse dust distribution. We found that we could

Table 1. Fixed Model Parameters

Name	M_* (M_\odot)	R_* (R_\odot)	T_{eff} (K)	r_{box} (au)	h_{box} (au)	i (deg)	PA (deg)	χ_R ($\text{cm}^2 \text{g}^{-1}$)	κ_P ($\text{cm}^2 \text{g}^{-1}$)	κ_P^* ($\text{cm}^2 \text{g}^{-1}$)	χ_P^* ($\text{cm}^2 \text{g}^{-1}$)
HD 163296	2.04 _a	1.6 _b	9300 _b	30-150	67.9	46.9	135.8	2.7	1.5	2.7	17.2
DoAr 44	1.4 _c	1.85 _d	4760 _c	15-80	25.7	17.7	58.0	2.7	1.5	1.4	12.0

References—*a.* Andrews et al. (2018), *b.* Fairlamb et al. (2015), *c.* Cieza et al. (2021), *d.* Ricci et al. (2010)

not use this approach to recreate the sharpness of the rings that are observed in the ALMA data of HD 163296. Instead, we found that the substructure in HD 163296 is better modeled as distinct rings rather than gaps carved into an unperturbed disk. We formed Gaussian shaped rings in the surface density profile, which gave us the ability to fine-tune the thin rings of HD 163296 and the ring-skirt morphology of DoAr 44.

This approach is no longer dependent on the density profile from the unperturbed disk since the Gaussian profiles are inserted into an otherwise empty density profile. The temperature structure from the unperturbed disk model is used initially, but it is then recalculated by the JC2008 code to agree with the new surface density profile. The code then recalculates the vertical density profile in order to restore hydrostatic equilibrium, and then continues to iterate with the disk temperature until steady-state is achieved.

Two Gaussian rings were used to fit the rings observed in HD 163296. However, our simulation box, covering 30–150 au, also contains a portion of the inner disk and very faint emission beyond the second ring. In order to best replicate the environment surrounding the two rings, we add two additional rings with fixed parameters at the boundaries of our model. The parameters for these “boundary rings” (Ring IDs 0 and 3 in Table 2) were determined from previous characterization of the disk’s thermal emission (Isella et al. 2018).

Ring 0 is necessary to recreate the inner disk interior to the two rings. The density along the interior edge is linearly extrapolated to fill in the disk interior between the inner radius of the simulation box and one-tenth of that inner radius. This is between 3 and 30 au for the HD 163296 model. The surface of the disk is extrapolated within this region using a radial power-law. The ALMA data show that there is an additional subtle peak in thermal emission just beyond our simulation box at 159 au (Isella et al. 2018). We added Ring 3 to best match this observation and add flexibility to our model, but we found that it has no noticeable effect on the primary rings (1 & 2) of our model.

Because we are only interested in modeling the rings of HD 163296 for this investigation, we apply masks to the additional thermal emission from the disk when finding

the best-fit model. This includes the disk interior to ~ 45 au and the asymmetric arc around 55 au in the south-east side of the disk (Figure 1). The masks are shown in Figure 2 and Figure 3.

For DoAr 44, three rings with significant overlap were used to recreate the three prominent portions of the ring-skirt morphology: inner skirt, bright central ring, and outer skirt. No additional rings were used at the edges of the simulation box because of the cavity and absence of observable thermal emission beyond the outer skirt in the DoAr 44 data. We avoid zero density errors by linearly extrapolating the density at the interior of the model from 1.5 to 15 au. The very low density at the edge of the box is thus decreased even further towards the star without creating a true void.

3. RESULTS

3.1. Model Fitting to HD 163296

From our grid-based search of Gaussian parameters, we found a best-fitting model to the ALMA observation of HD 163296. The general form of the dust surface density (Σ_d) profile, expressed as a summation of the Gaussian ring components, is as follows:

$$\Sigma_d(r) = \sum_i \Sigma_{d,i} e^{-(r-a_i)^2/2\sigma_{r,i}^2}. \quad (1)$$

The parameter ranges explored for radial position a , peak dust surface density Σ_d , and ring width σ_r of the inner ring were 63.1–72.1 au, 0.3–0.7 g cm^{-2} , and 2–6 au, respectively. For the outer ring, we searched $a = 94.6$ –110.6 au, $\Sigma_d = 0.1$ –0.6 g cm^{-2} , and $\sigma_r = 2.7$ –6.7 au. The best-fitting values were determined by minimizing the residuals between the synthetic thermal emission from the models and the ALMA data (Table 2). After a preliminary fit to find the approximate best fit, we fully explore the parameter space up to at least 5 standard deviations from the approximate best fit along each parameter axis. The fixed ring parameters in Table 2 are used for all models of HD 163296 to set the boundary conditions of the model disk at 30 au and 150 au. The parameters are based on fits to the surface brightness in the ALMA data (Isella et al. 2018).

The surface density of the disk is converted to a surface brightness via the image construction portion of

Table 2. Best-Fitting Model Results

Disk	Ring ID	a (au)	Σ_d (g cm $^{-2}$)	σ_r (au)	M_d (M_\oplus)	T_m (K)	H (au)
HD 163296	0	30	0.86	4.4
HD 163296	1	$67.9^{+0.5}_{-0.6}$	0.50 ± 0.09	$4.1^{+0.7}_{-0.5}$	81 ± 13	$35.5^{+1.4}_{-1.7}$	$4.6^{+0.1}_{-0.2}$
HD 163296	2	$102.6^{+0.9}_{-1.1}$	$0.29^{+0.13}_{-0.06}$	$4.7^{+1.4}_{-1.8}$	82^{+26}_{-16}	$28.5^{+0.7}_{-1.1}$	$7.8^{+0.3}_{-0.1}$
HD 163296	3	159	0.026	10
DoAr 44	1	$41.7^{+1.4}_{-3.5}$	$8.4^{+1.2}_{-1.5} \times 10^{-2}$	$9.0^{+1.9}_{-0.8}$	$18.4^{+3.1}_{-2.1}$	$28.4^{+0.6}_{-1.1}$	2.45 ± 0.13
DoAr 44	2	$47.1^{+0.8}_{-0.9}$	$12.8^{+4.5}_{-3.1} \times 10^{-2}$	$2.8^{+0.9}_{-0.6}$	$9.8^{+3.4}_{-2.7}$	26.6 ± 0.7	2.82 ± 0.05
DoAr 44	3	$65.1^{+1.1}_{-2.4}$	$14.7^{+2.2}_{-1.9} \times 10^{-2}$	$10.0^{+3.5}_{-2.3}$	$55.4^{+17.5}_{-11.1}$	$18. \pm 0.5$	$4.05^{+0.09}_{-0.04}$

NOTE—Ring ID refers to the index, i , in Equation 1. The boundary parameters for HD 163296 (Rings 0 and 3) were held constant for all parameter searches, and therefore are not given solutions for the output variables (dust mass, midplane temperature, and scale height).

the radiative transfer code (Jang-Condell 2009). Figure 2 shows a comparison of the thermal emission from the ALMA data (a) and the model (b). Each image has a mask applied to the central disk and the south-east arc interior to the first ring (Figure 1) so that these regions are excluded from our determination of best fit. The best-fit model of the rings in HD 163296 show no overlap and relatively tight radial dispersions ($\sigma_r < 5$ au). The radial locations of the model rings are well matched to the observation, but the purely Gaussian rings and absence of noise in the model give a smoother appearance.

Figure 3 compares the the GPI data (a) to polarized scattered light of the same model (b). A mask is only applied to the central disk since the arc does not appear in scattered light. Because the best-fitting model was determined purely by the ALMA data, there is a more significant difference between the scattered light observation and synthetic image.

In particular, the outer ring is not visible in the GPI observation. The offset of the center of the ring from the stellar location in Figure 3a suggests a scattering height, h , of roughly 11 au. Our model overestimates this scattering height to be approximately 18 au. This implies that the disk around HD 163296 likely has vertical dust settling for larger grains, which the model does not consider, leading to a smaller h/r fraction in the outer ring than the inner ring (i.e., $h \lesssim 16.5$ au in the outer ring). This is discussed more in Section 7.

The azimuthally averaged dust surface density, thermal emission, and scattered light are compared in Figure 4. The slight deviation of the rings in thermal emission from purely Gaussian shapes is emphasized by the middle panel. In the bottom panel, we see that our model correctly predicts the slight misalignment of the inner ring in scattered light from the thermal emission and

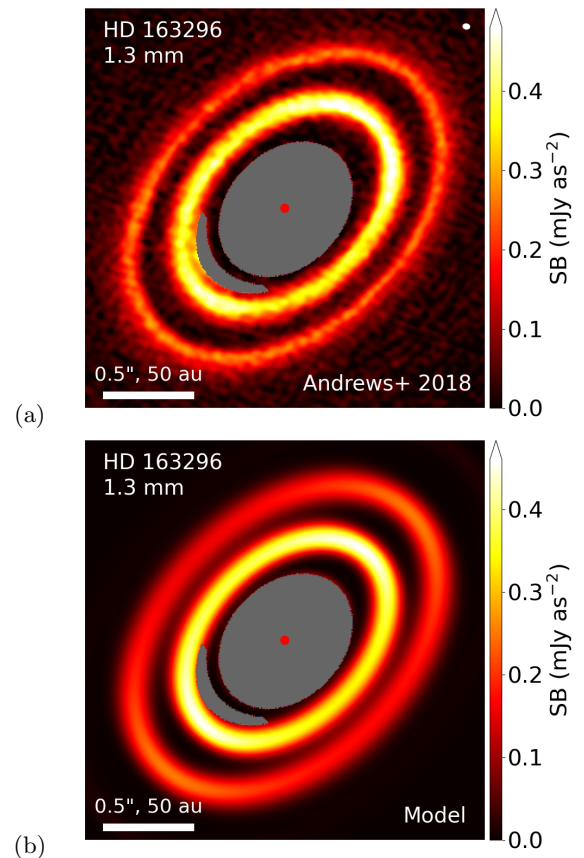


Figure 2. (a) ALMA image of the two rings in HD 163296, taken from Andrews et al. (2018) (b) thermal emission at 1.3 mm from our best-fitting model. The masks we applied to the inner disk and the region containing the asymmetric arc are shown in gray in both images. The approximate stellar location is marked with a red dot. An ellipse marks the beam size in the upper right of the ALMA observation.

peak surface density. The absence of the outer ring in the GPI observation is also illustrated.

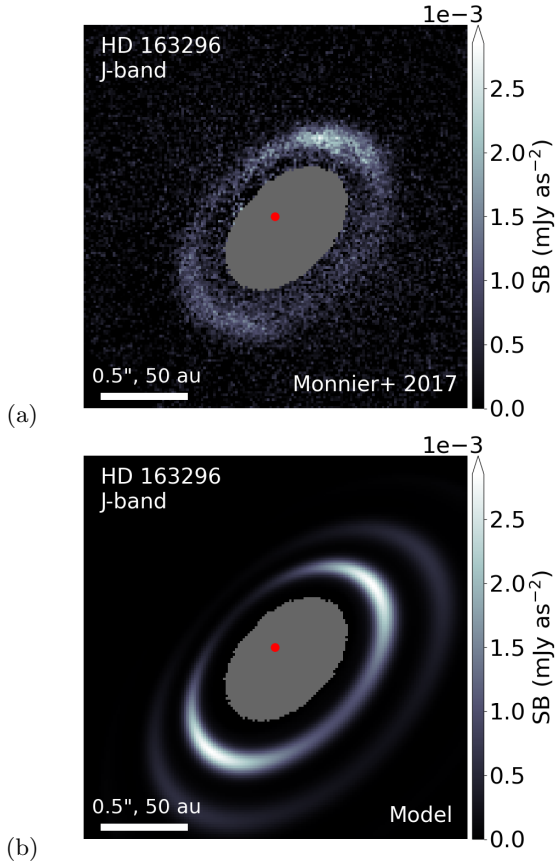


Figure 3. (a) GPI observation showing scattered light from the surface of the inner ring, taken from [Monnier et al. \(2017\)](#). (b) Synthetic scattered light image of the best-fitting model. We apply a mask to the central region (shown in gray). The approximate stellar location is marked with a red dot. The GPI data was not used to determine the best-fit model, so the brightness of the outer ring and the ring locations are different between the model and data.

The midplane temperature of the disk displays a complex behavior. There is an increase in temperature with radius in the first ring that continues outward into the gap between the rings (Figure 5). The outer ring is locally consistent with a monotonically decreasing profile. The midplane temperature from the model is generally similar to the power laws used in [Dullemond et al. \(2018\)](#) and [Doi & Kataoka \(2021\)](#). The shape of the profile is similar to the results from [Guidi et al. \(2022\)](#), though our profile is warmer overall.

We compare the difference in the azimuthal variation between the inner ring and outer ring observed with ALMA in Figure 6. The model of the inner ring predicts a flatter profile that is broadly similar to the observation. The model of the outer ring predicts a greater azimuthal variation due to the decrease in optical depth. However, the observation shows that the outer ring actually has a flatter profile. This deviation from the model is likely

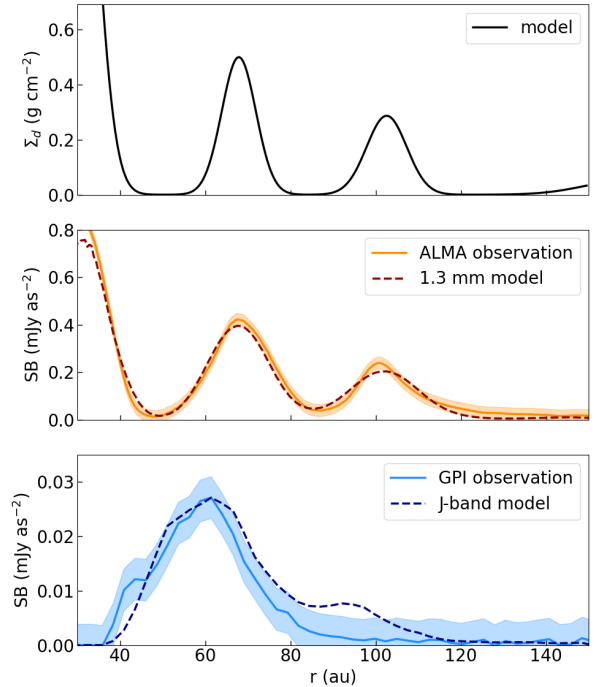


Figure 4. *Top:* Dust surface density of the best-fitting model to the ALMA observation of HD 163296. *Middle:* Surface brightness (SB) of ALMA observation with shaded errors and best-fitting model at 1.3 mm. *Bottom:* Surface brightness (SB) of GPI observation with shaded errors and the model in J-band.

related to the fact that the outer ring is not observed in the GPI data, which we discuss further in Section 7.1.

The model predicts some azimuthal asymmetries from the near and far side of the rings, which depend on the temperatures of the rings along the line of sight. The inner ring of the model is warmer at larger radii (Figure 7), so the line of sight to the near side of the ring passes first through a warmer region, while the line of sight to the far side of the ring passes first through a cooler region. Thus the near side appears brighter. Conversely, the outer ring is cooler at larger radii and therefore the opposite effect is observed.

We determine confidence limits for our best-fitting parameters by calculating $\Delta\chi^2$, which is the deviation of the χ^2 value for a set of model parameters from the best-fitting model (χ^2_{\min}), i.e. $\Delta\chi^2 = \chi^2(a, \Sigma_d, \sigma_r) - \chi^2_{\min}$. We scale the ALMA uncertainties such that the reduced-chi-square (χ_r^2) value of the best-fitting model is equal to one in order to help mitigate any misestimation of error-bars or unknown biases. By doing so, we enforce, a priori, that our measurement errors are consistent with χ^2_{\min} being close to the expected value. Because $\Delta\chi^2$ itself can typically be well-described by the χ^2 distribution (see, e.g., [Avni 1976](#)), 68.3% ($\sim 1\sigma$), 95.5%

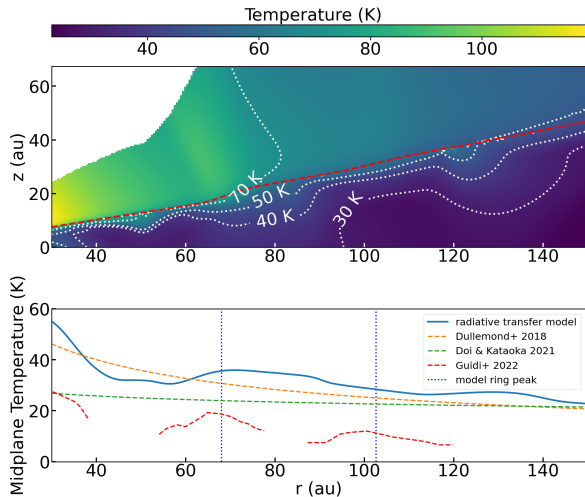


Figure 5. *upper:* Temperature map of the best-fitting model of HD 163296. The scattering surface of the disk, as determined by the model, is displayed as a dashed red line. Labeled isotherms are represented with dotted white lines. The very low density region in the upper left (displayed in white) does not conform to our model assumptions of well mixed dust and thermal equilibrium between dust and gas. Therefore, the temperature cannot be properly calculated by our model in this region. *lower:* Midplane temperature of the model compared to other studies (the temperature from Guidi et al. (2022) is not well constrained in the dust gaps). Our model ring locations are marked with vertical lines.

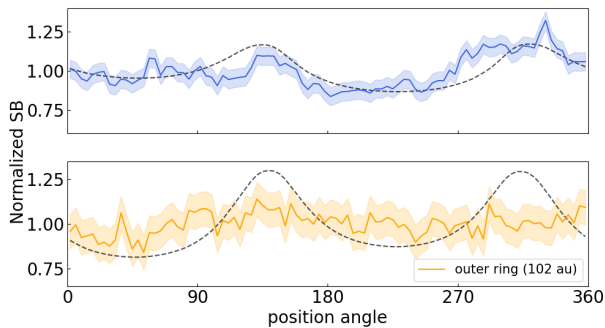


Figure 6. Azimuthal variation of normalized intensity of the rings around HD 163296 observed with ALMA. The curves were calculated by taking the peak surface brightness for each ring at every angle. The results are normalized to compare the relative deviations between different rings. Each ring observation is plotted in color, and the corresponding best-fitting model is depicted in dashed black lines. The uncertainty of the observations are plotted as colored envelopes. The outer ring shows a more distinct deviation from our model predictions.

($\sim 2\sigma$) and 97.7% ($\sim 3\sigma$) of the posterior probability for a three-parameter fit is expected to be contained within approximately $\Delta\chi^2 \leq 3.53$, $\Delta\chi^2 \leq 8.02$ and

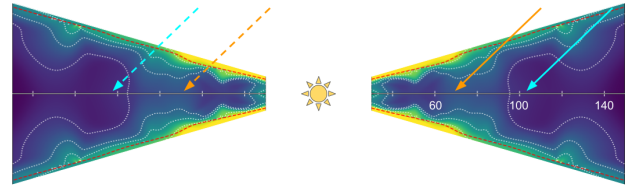


Figure 7. Schematic showing the temperature map from Figure 5 and the lines of sight to the near (solid) and far side (dashed) of the rings in the model. The temperature map has been cropped to just below the disk surface, and the contour labels have been removed for clarity. Labels are placed at 60, 100, and 140 au on the right hand side. The inner ring (orange) is warmer along the line of sight to the near side, while the outer ring (cyan) is warmer along the line of sight to the far side. This creates the respective asymmetries on the near and far sides of the disk in Figure 6.

$\Delta\chi^2 \leq 14.16$, respectively. Contour plots of the best-fit parameters based on confidence limits derived from $\Delta\chi^2$ are shown in Figures 8 and 9.

There is a degeneracy in goodness-of-fit for models with a particular relation of ring width to surface density (Figures 8c and 9c). Exchanging ring width for surface density such that total mass in the ring remains consistent can result in similar synthetic thermal emission images. Because of this relationship, the errors for a and Σ_d are much larger.

3.2. Model Fitting to DoAr 44

The same method of ring parameter searches was then applied to the ALMA observation of DoAr 44. However, the clear difference in morphology between the disks of DoAr 44 and HD 163296 requires a new approach to the Gaussian rings. The shape of the disk around DoAr 44 has been described as a bright ring with a skirt (Figure 10). We determined that the skirt itself is best fit by two separate Gaussian distributions for the inner and outer portion. Three sets of Gaussian parameters were used for the total disk: inner skirt, bright central ring, and outer skirt.

The general form of the equation for the dust surface density of the best-fitting model is again given in Equation 1 with the value and uncertainty of these parameters for DoAr 44 provided in Table 2. For ring 1, we searched the ranges $a = 37.0\text{--}47.0$ au, $\Sigma_d = 0.030\text{--}0.122$ g cm $^{-2}$, and $\sigma_r = 4.5\text{--}13.2$ au. For ring 2, we explored $a = 45.0\text{--}48.9$ au, $\Sigma_d = 0.055\text{--}0.235$ g cm $^{-2}$, and $\sigma_r = 0.08\text{--}5.3$ au. Finally, for ring 3, we searched $a = 60.4\text{--}67.0$ au, $\Sigma_d = 0.0880\text{--}0.238$ g cm $^{-2}$, and $\sigma_r = 3.9\text{--}15.0$ au.

The ALMA observation is compared to our best-fit model in Figure 10. Due to the cavity, a central mask in-

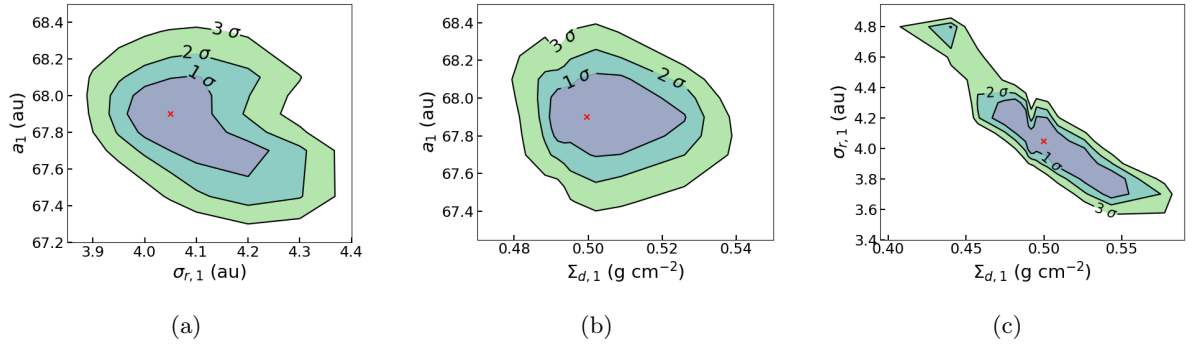


Figure 8. Contour plots of model χ^2 values for the parameters of the inner ring of HD 163296. Contours are plotted for 1σ (purple), 2σ (blue), and 3σ (green) deviations from the best fit. The best fit is marked with a red x in each plot. For each contour plot, the best fit value was used for the unplotted parameter. (a) and (b) show little correlated error between those variables, but there is a significant degeneracy in (c) between the ring width and surface density.

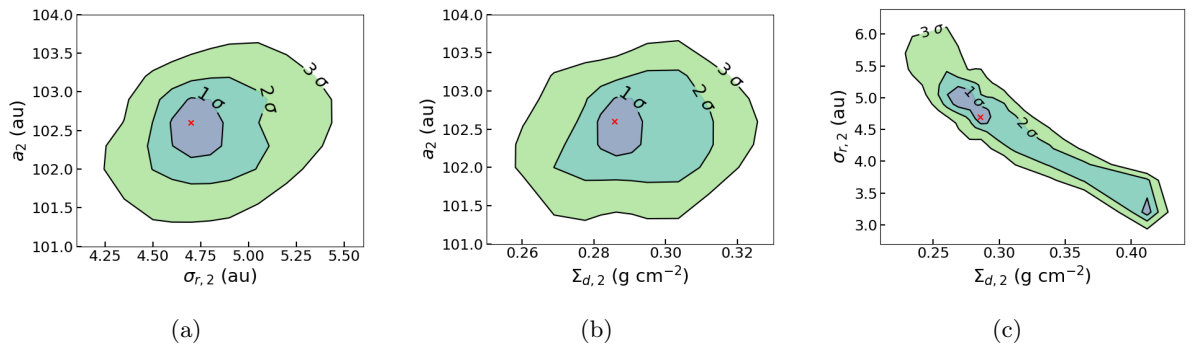


Figure 9. Same as Figure 8, but for the outer ring parameters

terior to our model’s 15 au inner edge was not necessary when fitting the data. We find that our three overlaid Gaussian rings give a good replica of the ring-skirt morphology observed in the ALMA data. The best-fit model uses two rings with larger radial dispersions ($\sigma_r \geq 9$ au) for the inner and outer portion of the skirt and one ring with a tight radial dispersion ($\sigma_r = 2.8$ au) for the bright ring.

The same model is then compared to the scattered light observations in Figure 11. The $0.1''$ coronagraph used in the observation is shown in both the observed and synthetic SPHERE data. We made no attempt to replicate the azimuthal variation of the SPHERE variation, which is likely the result of shadowing from a misaligned inner disk (Casassus et al. 2018). Ring 2 (the bright ring in thermal emission) is faintly visible in the scattered light model but not the observation. However, both observed and modeled scattered light images show peaks in emission that are interior to the cavity in thermal emission.

The surface density for the best-fitting model of DoAr 44 has a similar profile as the intensity from the thermal emission (Figure 12). The three overlaid Gaus-

sian rings are able to produce a good replica of the observed ring-skirt thermal emission morphology.

Our model shows a monotonic increase in scattered light towards the star despite the central cavity (Figure 12). The SPHERE data agrees that the peak scattered light emission occurs in the low density cavity. We note that the SPHERE data for DoAr 44 was not collected with any flux calibrators. We can only compare the morphology of the SPHERE data with our model. The relative flux of the SPHERE data was scaled to the intensity of our model.

Unlike the SPHERE data, our initial scattered light model does not show a local maxima around 20 au. The N.ALC.YJ.H.S coronagraph used during the SPHERE observation has an edge that extends out to $0.1''$, at which the coronagraphic response is 50% (Wahhaj et al. 2020). However, the full coronagraphic response doesn’t reach 100% transmission until $0.2''$. When we apply a similar coronagraphic response profile to our synthetic data, we find a local maximum at the 15 au edge of our box (Figure 12). The resemblance of this morphology to the SPHERE data and the complications of inferring data beyond the edge of our simulation are discussed in Section 7. We also note that the model shows a slight

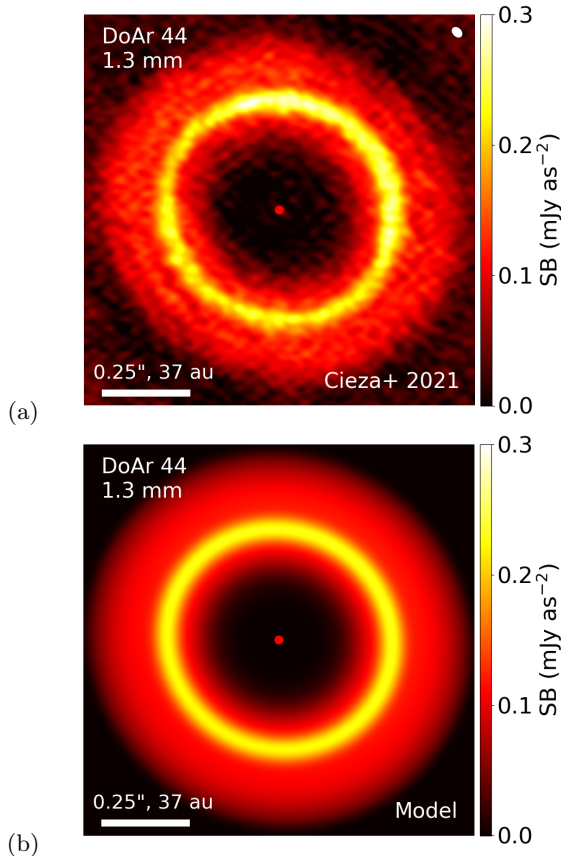


Figure 10. Surface brightness (SB) of the thermal emission from (a) the 1.3 mm ALMA image of DoAr 44 (Cieza et al. 2021) and (b) the synthetic 1.3 mm data from our best-fitting model. An ellipse marks the beam size in the upper right of the ALMA observation. The approximate stellar location is marked by a red dot. Modeling the ring-skirt morphology as three overlaid Gaussian rings gives a good replica of the ALMA observation.

bump at 47 au that is not seen in the SPHERE data. This is likely due to the gas and fine dust distributions not being as sharply peaked around 47 au as the larger dust distribution.

Unlike HD 163296, the midplane temperature in the model of the disk of DoAr 44 decreases monotonically with radius within the region we are investigating (Figure 13). The temperature of this model is cooler and begins to fall below 20 K in the outer disk. We note that stellar irradiation provides the only heating for the disk in our model. External radiation fields, which may begin to have a more considerable effect on temperature at large radii, are not included.

We investigate the difference between the azimuthal variation in the ALMA data and our model at the bright ring of DoAr 44. Figure 14 shows that the model predicts a relatively flat profile, particularly when compared to HD 163296 (Figure 6). DoAr 44 has a lower inclina-

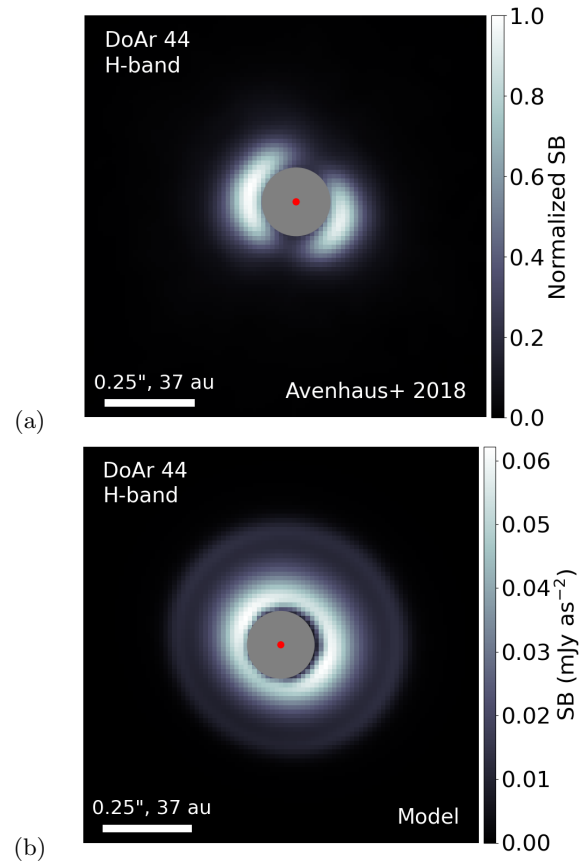


Figure 11. (a) H-band SPHERE image of DoAr 44 (Avenhaus et al. 2018) and (b) synthetic data of scattered light from our best-fitting model. The surface brightness (SB) of the SPHERE data has been normalized since the data are not absolute flux calibrated. The $0.1''$ SPHERE coronagraph (shown in gray) is displayed on both the H-band observation and the synthetic data. The approximate stellar location is marked by a red dot. The scattered light of both the disk and the best-fit model peak inside of the cavity in thermal emission.

tion than HD 163296 (17.7° and 46.9° , respectively), which results in only small changes in viewing angle around the disk. However, the observation of DoAr 44 shows a distinct brightening on the north-west side of the disk ($\sim 250^\circ$ – 20°). This may be the result of an excess of mm-sized dust on that side of the disk, which we discuss further in Section 6.1.

The confidence limits for the best-fitting parameters of DoAr 44 to the ALMA data were determined using the same method as the confidence limits for the parameters of HD 163296. However, in this case we use a nine-parameter fit because the overlap between rings prevents fitting each ring individually. We therefore use 68.3% ($\sim 1\sigma$), 95.5% ($\sim 2\sigma$) and 97.7% ($\sim 3\sigma$) of the posterior probability for a nine-parameter fit, which are expected to be contained within approximately $\Delta\chi^2 \leq 10.4$,

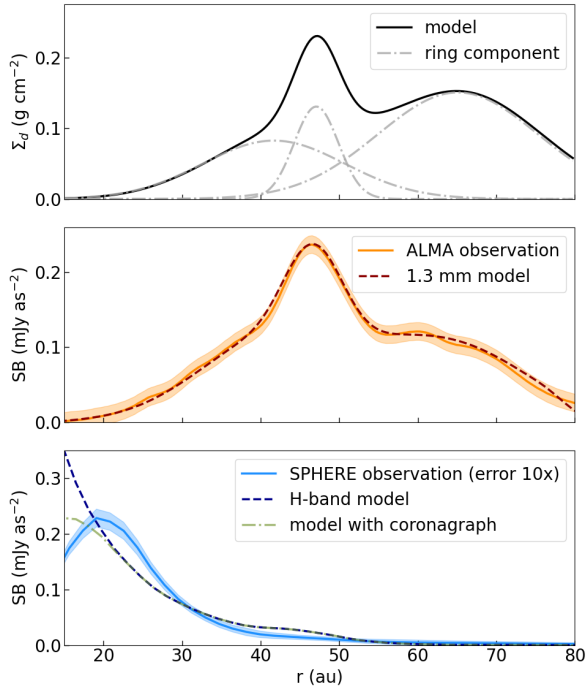


Figure 12. *Top:* Dust surface density of the best-fitting model to the ALMA observation of DoAr 44. The three separate ring components are depicted as dashed lines. *Middle:* Surface brightness (SB) of ALMA observation with shaded errors and the model at 1.3 mm. *Bottom:* Surface brightness (SB) of the SPHERE observation with shaded errors shown at $10\times$ magnification (in order to be seen) and the model in H-band. An additional model with a coronagraphic response function similar to the SPHERE data is also shown. The SPHERE data are not flux calibrated, so they have been scaled to the same maximum value as our model with the coronagraphic response. Dimmer regions of the SPHERE observation have been excluded from this azimuthal average.

$\Delta\chi^2 \leq 17.2$ and $\Delta\chi^2 \leq 25.3$, respectively. The overlap between the individual rings also creates a degeneracy in ring parameters that can produce the same surface density values, particularly for ring 2 at 47 au. Figure 15 shows some selected contours from our χ^2 -fitting that best emphasize the range of degeneracy between $\Sigma_{d,2}$ and other ring parameters.

4. ESTIMATING DUST MASS

Mass estimates for the disks depend strongly on the dust opacity and disk temperature assumed in the models. Assuming blackbody radiation and an optically thin approximation, the derived dust mass in the disk scales as $M_d \propto 1/\kappa_\nu^{\text{abs}}$ and $M_d \propto T^{-1}$. Here κ_ν^{abs} refers specifically to the opacity of dust alone. These simplified scaling relationships do not account for degeneracies in grain composition or shape. To date, there remains a significant uncertainty in the dust opacities.

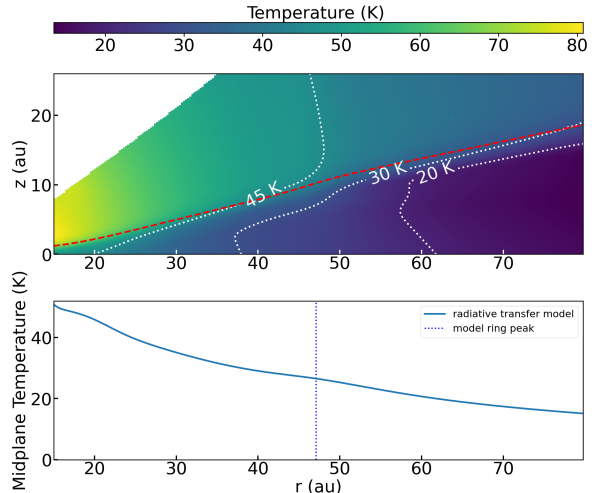


Figure 13. *upper:* Temperature map of the best-fitting model to the ALMA observation of DoAr 44. The scattering surface of the disk is displayed in red. Labeled isotherms are shown with dashed white lines. As with Figure 5, there is a significantly low density region in the upper left for which the temperature cannot be properly using our model assumptions. *lower:* Midplane temperature of the model. There is a subtle increase in temperature around the model’s peak surface density at the bright middle ring.

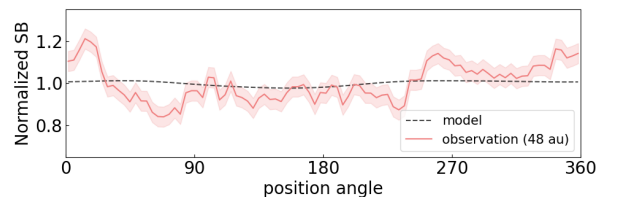


Figure 14. Azimuthal variation of the normalized surface brightness (SB) of the bright ring around DoAr 44 observed with ALMA. The figure formatting is the same as Figure 6.

Regions of disks have been observed in the DSHARP survey with intermediate to high optical depths, even at large radii (Birnstiel et al. 2018). Mass estimates for the rings in this case becomes a very non-trivial task. However, we find that our mass estimates for the rings in HD 163296 are comparable to previous studies (Table 3).

Furthermore, different methods for determining the dust mass may affect the results. Dullemond et al. (2018) find the dust distribution for HD 163296 from deconvolved Gaussian fits to the intensity profile under the assumption of a fixed temperature profile. Doi & Kataoka (2021) use RADMC-3D (Dullemond et al. 2012) to find a best fit with the DSHARP opacity model (Birnstiel et al. 2018) and a fixed temperature profile. Rab et al. (2020) found a fit to the $^{12}\text{CO } J = 2 - 1$ line

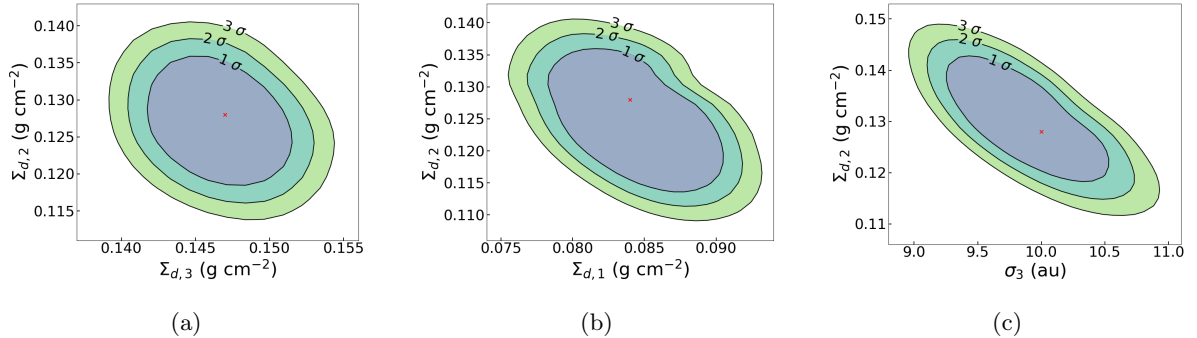


Figure 15. Selected contours from χ^2 -fitting that demonstrate correlation of $\Sigma_{d,2}$ vs. $\Sigma_{d,3}$ (a), $\Sigma_{d,1}$ (b), and σ_3 (c). Contours are plotted for 1σ (purple), 2σ (blue), and 3σ (green) deviations from the best fit. The best fit is marked with a red x in each plot. For each contour, the unused ring parameters are set to their best-fit values. Each contour shows some degeneracy between the variables, but it is most clearly demonstrated in (c).

Table 3. Dust Mass Estimates of HD 163296 rings

Study	$\kappa_{1.3\text{ mm}}^{\text{abs}}$ ($\text{cm}^2 \text{ g}^{-1}$)	inner ring		outer ring	
		M_d (M_{\oplus})	T_m (K)	M_d (M_{\oplus})	T_m (K)
this study	0.90	84 ± 14	35.5	81.5 ± 17	28.5
(1)	2.0	56.0	30.8	43.0	25.3
(2)	0.48	200	24.0	135	22.6
(3)	1.24	~ 75	~ 20	~ 80	~ 18
(4)	~ 2	53	21.4	96	12.1

NOTE—Previous studies: (1) Dullemond et al. (2018), (2) Doi & Kataoka (2021), (3) Rab et al. (2020), (4) Guidi et al. (2022).

and the 1.3 mm continuum using a radiation thermochemical disk code. Guidi et al. (2022) performed a multi-wavelength study and used a physical model with an analytical expression for radiative transfer that assumes isotropic scattering from an isothermal slab.

Avenhaus et al. (2018) estimates the total dust mass in the disk of DoAr 44 as $39 M_{\oplus}$, assuming an optically thin disk, a constant disk temperature of 30 K, and dust opacity of $2.3 \text{ cm}^2 \text{ g}^{-1}$. For the dust mass, we find $M_d = 84_{-3.5}^{+7.0} M_{\oplus}$ in the 15-80 au region. The bulk of the disk mass is located in regions of the disk that are closer to 20 K in our model with a dust opacity of $0.9 \text{ cm}^2 \text{ g}^{-1}$. The scaling relationship of calculated dust mass with temperature and dust opacity accounts for much of the difference in the two mass estimates.

5. POTENTIAL EMBEDDED PLANETS

Embedded protoplanets have not yet been directly detected around either HD 163296 or DoAr 44. The disk structures from our radiative transfer models allow us to further constrain mass ranges for putative planets in these disks.

5.1. HD 163296

The rings and gaps in the disk around HD 163296 are well explained by embedded planets. Recent analysis of CO channel maps reveal two kinematic deviations likely caused by planets in the disk: a $1 M_J$ planet around 94 au (Izquierdo et al. 2021) and a $2 M_J$ planet around 260 au (Pinte et al. 2018). While a third kinematic deviation has not yet been detected, an additional planet may yet be the cause of the inner gap around 50 au. It is also possible under the assumption of low-viscous transport that a single planet may open multiple gaps in the disk (Bae et al. 2018).

We assume that both gaps in the disk may be caused by individual planets. Using the parameters from our best-fitting model, we estimate the planet mass using the method from Crida et al. (2006). In order for a planet to form gaps with depths below 10% of the background surface density, it must possess a dimensionless parameter $\mathcal{P} \leq 1$, where \mathcal{P} is defined as

$$\mathcal{P} = \frac{3H}{4r_h} + \frac{50}{q\mathcal{R}}. \quad (2)$$

Here, r_h is the planet's Hill radius, q is the planet-star mass ratio, \mathcal{R} is the Reynolds number, and H is the scale height. We use the density scale height $H = \Sigma / (\sqrt{2\pi}\rho(z=0))$. In the formulation from Crida et al. (2006), the Reynolds number is defined as $\mathcal{R} = r_p^2 \Omega_K / \nu$ and, therefore, depends on the planet's orbital radius r_p and the viscosity ν . The viscosity is typically simplified with a viscosity parameter α (Shakura et al. 1978) such that $\nu = \alpha c_s H$.

Our model of HD 163296 with prominent rings and deep gaps is best fit to the mm-sized dust distribution, not the gas distribution. CO observations show that the gas does not have the same level of depletion in the gaps (Isella et al. 2016). If we instead use the condition that the gas gaps do not fall below 10% of the background

surface density ($\mathcal{P} \geq 1$), we can then calculate upper limits for planet masses.

The presence of dust gaps in HD 163296 still provides a lower limit on the possible planet masses, despite the absence of gas gaps. A planet that reaches the pebble isolation mass, $M_{\text{iso}} \sim 0.2M_{\text{th}} \sim M_*(H/r_p)^3/2$, is capable of forming a pressure bump that causes a dust gap (Lambrechts et al. 2014; Rosotti et al. 2016). Here, M_{th} is the gap opening mass given by the thermal criterion, according to which $r_h \gtrsim H$. Using both the conditions for the presence of dust gaps, but the absence of gas gaps, we can set both upper and lower bounds on the possible planet masses in HD 163296 for a range of α values (Figure 16).

In the lower viscosity regime, we estimate mass ranges of 0.4–0.8 M_J and 0.9–2 M_J for the possible inner and outer planets respectively. This mass range for the outer planet agrees with the 1 M_J derived from kinematic deviations in CO velocity channels (Izquierdo et al. 2021). The mass upper limits are not bounded for the higher viscosity regime.

5.2. DoAr 44

A planet also provides a likely formation mechanism for the cavity in the disk of DoAr 44. A planet that creates a deep gap in the disk may then prevent inward mass flow, causing the disk interior to its orbit to become depleted. Our best-fit model for DoAr 44 finds that the gas depleted cavity still has a peak in scattered light within it, which agrees with the SPHERE observation. While the gas distribution is likely smoother than the distribution of larger dust grains around the bright ring, our gas depleted cavity in the model is capable of producing similar results to the SPHERE observations in scattered light. Therefore, we apply the condition $\mathcal{P} \leq 1$ to the cavity of DoAr 44.

We set the planet location to be 25 au, where the dust surface density falls to 10% of the peak value. We use the model parameters at this location to calculate the minimum planet mass that may be responsible for this cavity. We again perform this calculation as a function of α (Figure 16). In the low viscosity regime, we find a minimum mass for all α values of approximately 0.5 M_J for a planet to form the cavity in DoAr 44.

Unlike HD 163296, DoAr 44 has a cavity in both gas and dust distributions. Therefore, we cannot use the same condition to calculate an upper mass limit for a planet in DoAr 44. Instead, we can place upper limits on the potential planet based on the non-detection of a surrounding circumplanetary disk (CPD) in the ALMA observation of DoAr 44. We follow the prescription from Pineda et al. (2019) for these calculations.

We first consider the case of an optically thin CPD, for which we are able to calculate an upper mass limit of the CPD. We use a 3σ sensitivity of $F_\lambda = 78 \mu\text{Jy}$ as the upper limit for a point source (Cieza et al. 2021). We assume the CPD would have an average temperature $T_d = 40$ K at 25 au such that the CPD is in thermal equilibrium with the surrounding environment. Finally, using $d = 146.3$ pc, $\lambda = 1.3$ mm, $\kappa_\lambda^{\text{abs}} = 0.9 \text{ cm}^2 \text{ g}^{-1}$, and the model dust-to-gas ratio $f_d = 0.0138$, we calculate the upper limit for the mass of an optically thin CPD:

$$M_{\text{CPD, thin}} \leq \frac{d^2 F_\lambda}{B_\lambda(T_d) \kappa_\lambda f_d} = 3.5 M_\oplus. \quad (3)$$

For comparison, a CPD candidate embedded in the disk around AS 209 has been determined to have a gas mass $\gtrsim 30 M_\oplus$ from observations of ^{13}CO emissions (Bae et al. 2022). The non-detection of continuum emission near the location of the CPD in AS 209 indicates a dust mass $\lesssim 0.027 M_\oplus$, which corresponds to a low dust-to-gas ratio of $\lesssim 9 \times 10^{-4}$. Though the putative CPD in the disk around AS 209 is located at a larger radius (~ 200 au), it is possible that a CPD in the DoAr 44 cavity could similarly have a diminished dust-to-gas ratio and therefore, if optically thin, a larger upper mass limit.

In the optically thick case, we are instead able to calculate the upper limit of the radius of a CPD. The calculation is derived from the equation $F_\lambda = B_\lambda(T_d)\Omega$, where Ω is the solid angle subtended by the disk. Using the same values from equation 3, we find an upper limit on the radius for a optically thick CPD at 25 au to be:

$$R_{\text{CPD, thick}} \leq d \sqrt{\frac{F_\lambda}{\pi B_\lambda(T_d)}} = 0.6 \text{ au} \quad (4)$$

We assume that the CPD would extend to this radius, so we set 0.6 au as the disk truncation radius ($\sim 1/3$ the Hill radius). From this, we calculate an upper limit on the planet mass to be 1.6 M_J . An optically thick CPD around a more massive planet would therefore be large enough to detect. Though it is difficult to constrain an upper mass limit for a planet that suits every scenario, we find a tight constraint of 0.5–1.6 M_J (Figure 16) for the special case of an optically thick CPD around a planet.

6. EXPLANATIONS OF DOAR 44 MORPHOLOGY

Disk cavities are promising indicators for embedded planets in disks. However, a single planet in the cavity around DoAr 44 would be insufficient to produce the ring-skirt morphology. Some additional mechanism is

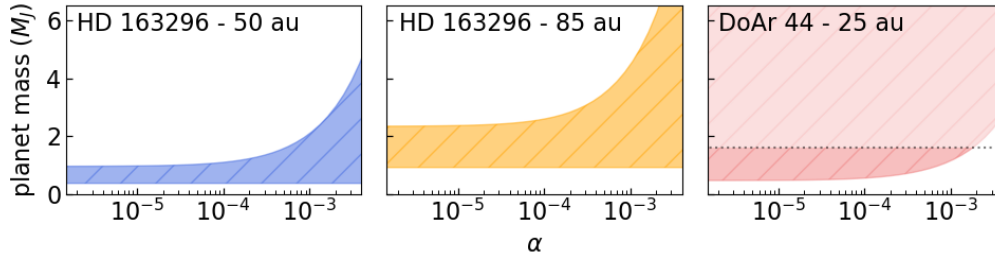


Figure 16. Mass limits on the possible planets at 50 au (*left*) and 85 au (*center*) around HD 163296 as a function of the viscosity parameter α . A lower mass limit on planet masses in DoAr 44 (*right*) that would be massive enough to create the observed cavity. The dashed line at $1.6 M_J$ represents a tentative upper limit for putative optically thick circumplanetary disk.

needed to create an accumulation of coarse dust grains at the bright ring.

6.1. Giant Impact Scenario

One possible explanation for the bright ring is a giant impact near that radial location. If the cavity of DoAr 44 indicates that the disk is entering the transition phase, then we could expect solid bodies to begin colliding more frequently. Catastrophic impacts can release a significant mass fraction of the progenitor bodies as debris via a collisional cascade (Leinhardt & Stewart 2012).

The bright ring in DoAr 44 has a relatively flat azimuthal profile, as expected from the disk’s lower inclination (Figure 14). However, there is an asymmetry in the two sides of the disk that our radiative transfer model does not reproduce. Figure 14 shows that the north-west side of the disk (position angles $\sim 250\text{--}20^\circ$) is consistently brighter than the model predicts. The asymmetry may be the result of excess dust produced in a giant impact that has since been smeared out into a nearly axisymmetric distribution.

From the range of surface densities we explored in our model, we determine that the asymmetry could be produced by a 15% change in Σ_d from one side of the disk to the other. This corresponds to roughly $1 M_\oplus$ of excess dust on the north-west side of the disk. The mixing timescale of this dust would approximately be the timescale for the inner side of the ring to make a full orbit relative to the outer side. This corresponds to roughly 10^4 yr.

This short lifetime would make the asymmetry in the disk a transient event that is unlikely to be observed. Furthermore, giant impacts are more likely to occur after the gas is depleted, removing its damping effects on the planet and planetesimal orbits. The CO data of van der Marel et al. (2016) show this is not the case at the bright ring in DoAr 44.

6.2. Dust Drift Scenario

As an alternative explanation for the formation of the bright ring, we show that the DoAr 44 disk’s bright, narrow ring inside a skirt is a natural if transient outcome of dust particles drifting under drag forces in a gas surface density profile with a broad peak.

We consider the particular gas profile shown in Figure 17, combining a Gaussian with dispersion $\sigma_r = 15$ au inside the peak and a broader Gaussian with dispersion $\sigma_r = 30$ au outside the peak. For this model, the peak where the two sides connect is at 52 au. The gas must have a steeper pressure gradient on the cavity side in order to make the inner skirt narrower than the outer skirt. Such a gas asymmetry could come from a planet orbiting in the disk’s central cavity.

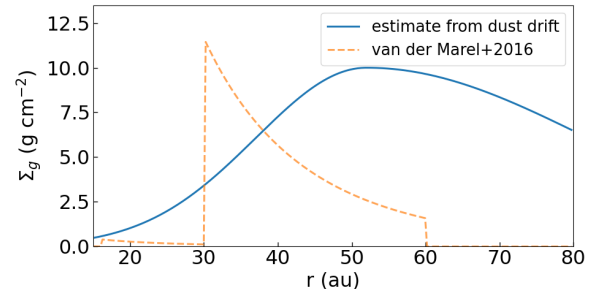


Figure 17. An estimate for a gas distribution that may create an accumulation of mm-sized dust into a bright ring similar to the ALMA observation of DoAr 44. For comparison, we also plot the profile fit by van der Marel et al. (2016) to ALMA CO observations.

The DoAr 44 disk’s gas surface density profile was also inferred by van der Marel et al. (2016) from ALMA observations of lines of ^{13}CO and C^{18}O . The gas was assumed to have a radial power-law structure with an exponential cutoff. The best-fit carbon monoxide isotopologue profile is shown in Figure 17 alongside our trial profile. We believe the smoothing from the large beam size ($\sim 0.25''$, 37 au) of their observation and the assumption of a decreasing power law in van der Marel

et al. (2016) explain much of the difference between the shape of their gas distribution and our estimate. Furthermore, the cut-off in their gas distribution at 60 au is near the expected CO snowline. CO condenses at temperatures of 23-28 K (Zhang et al. 2015), found in our model at 43 to 55 au. Finally, the total gas masses from the two sources depend on the assumed ratios of dust to gas and of CO to H₂.

Using the code `two-pop-py` (Birnstiel et al. 2012), we calculate the dust drift inside of the gas distribution from Figure 17. This code simulates the dust evolution by treating dust growth, fragmentation, and transport in a viscously evolving disk. The mass transport is calculated via advection-diffusion, with advection dominated by the drift produced by the difference between the orbital speeds of the dust and gas. Dust growth rate, and thus radial drift rate, depend on the choice of the viscosity parameter α . We use $\alpha = 3 \times 10^{-4}$ because it results in both a lower drift rate and an upper limit on the dust size exceeding 1 mm, consistent with the brightness of the disk’s mm-wave thermal emission. The fragmentation limit on particle size is inversely proportional to α . A larger α results in smaller particles that consequently drift more slowly, and vice versa. The temperature of the disk is taken from the midplane of our best-fit radiative transfer model.

We initialize the dust radial distribution to match that of the gas but with a surface density 100 times less. The initial grain size is 1 μm , but the code calculates grain growth for larger grains as the dust evolves. The particles fragment when they collide at $\geq 250 \text{ cm s}^{-1}$, an intermediate between values measured for silicate and water-ice-silicate particles in the laboratory (Blum & Wurm 2008; Gundlach et al. 2011). The gas distribution is static in our simulation. We find that the dust very quickly drifts to produce a peak around 50 au (Figure 18). At 50,000 years, the peak is quite similar to our radiative transfer model that best fits the ALMA dust continuum image.

We find that a more complicated gas distribution can better replicate our best-fitting dust model, particularly if we include an additional change in pressure gradient around 65 au. However, we do not wish to invoke an overly detailed model for a simple proof of concept. A limitation of this picture is the short lifetime of the ring-skirt morphology in the mm-sized dust. The ring becomes narrower than observed after about 50,000 years, which would make this a relatively transient event. Allowing for a smaller maximum grain size (e.g., 200 μm from Guidi et al. (2022)) would slow the drift, but results in a smoother coarse dust distribution. Possibly

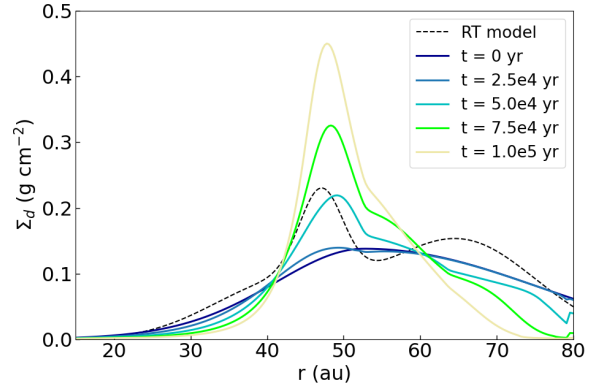


Figure 18. The evolution of the dust surface density over 10^5 years using the gas distribution from Figure 17. The dust distribution from our best-fitting radiative transfer (RT) model to the ALMA data (Figure 12) is plotted as a dashed black curve. We find that dust drift alone can produce a similar distribution after $\sim 50,000$ years.

tuning the other model parameters could reproduce the bright ring, but that is beyond the scope of this work

We also report the drift timescales as r/\dot{r} at the start of the time evolution for various grain sizes within this gas distribution (Figure 19). We find that larger grains ($\gtrsim 0.1 \text{ mm}$) will accumulate into the bright ring but smaller grains ($\lesssim 0.1 \text{ mm}$) will drift through and into the cavity. Therefore, in order to obtain the ring-skirt morphology for this chosen gas distribution, particles bigger than 0.1 mm are required.

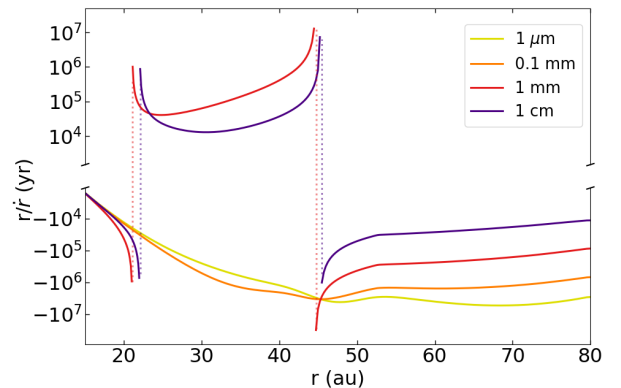


Figure 19. Dust drift timescales (r/\dot{r}) for various grain sizes within the gas distribution from Figure 17. The selected size range represents the range of grain sizes that grow over time in Figure 18. Dotted lines help line up the discontinuities between sign changes in drift rates. Positive and negative values correspond to outward and inward drift respectively. Grains smaller than 0.1 mm would not be trapped in the bright ring and may flow into the cavity.

7. SCATTERED LIGHT

The best fits for HD 163296 and DoAr 44 were determined using the ALMA data alone. In this context, the scattered light data provide supplementary info on the difference between our model and the disks themselves. The scattered light data do not contribute to the best-fitting model parameters.

7.1. HD 163296: non-convergence and dust settling

We were unable to find a best-fit model for HD 163296 based on the GPI data alone. We consider several reasons why we are less successful with the GPI data than the ALMA data. First, the GPI data and the synthetic data have different azimuthal variations in the observed polarized light. In the GPI observation, the ansae of the ring in the north-west (upper-right) and south-east (lower-left) do not have the same brightness, which our model does not replicate (Figure 3). This may be the result of forward or backward scattering of the light by fine dust grains at the surface. The anisotropy could then be described by a single parameter phase function, as in the Henyey-Greenstein function (Henyey & Greenstein 1941). However, in the Mie regime the scattering function becomes complex and the degree of polarization may no longer be symmetric to forward and backward scattering (Brunngräber & Wolf 2019). For this reason, we do not overextend our fitting parameters to include effects from azimuthal variation of the polarization scattering phase function.

Furthermore, the GPI observation and the models have significantly different polarization factors. The GPI data has a J-band polarization factor of $P_J = 0.008$ (Monnier et al. 2017). By comparison, the synthetic data has a much larger polarization factor of $P_J = 0.3$. The degree of polarization is highly sensitive to the incline of the disk surface. Figure 3 demonstrates that there are differences between the disk’s and our model’s surfaces. We can manually adjust the percentage of polarized light in our model, but that does not address the original issue of differing azimuthal variation between the model and observation. An in-depth study of the polarization is beyond the scope of this paper.

Most importantly, our code assumes that the dust is well mixed vertically. However, at this stage of disk evolution, most of the larger grains will have settled toward the midplane. There are several pieces of evidence that some amount of vertical settling has already occurred. First, the outer ring of HD 163296 in the ALMA data has a distinct lack of azimuthal variation compared to the prediction from our model (Figure 6). This flat profile indicates a more settled ring with a smaller aspect angle and therefore a smaller difference in local viewing

angle along the ring (Doi & Kataoka 2021). Second, the outer ring is not visible in the GPI data. This could be the result of shadowing if the μm -sized grains have settled to a lower height.

In order to consider the impact from dust settling, we calculate the timescales for various grain sizes to settle in the outer ring. Following the description from Dullemond & Dominik (2004), we find the equilibrium height of the dust from the settling time, t_{sett} , and the stirring time, t_{stir} . The settling time at a height z is determined by the terminal velocity, v_{sett} , of the dust particles, assuming Epstein drag occurs:

$$t_{\text{sett}} = \frac{z}{v_{\text{sett}}} = \frac{4\sigma\rho c_s}{m\Omega_K^2}, \quad (5)$$

where σ is the grain cross section, c_s is the sound speed, m is the grain mass, and Ω_K is the Keplerian frequency. t_{stir} is determined by the timescale for diffusion:

$$t_{\text{stir}} = \frac{z^2}{D} = \frac{\text{Sc} z^2}{\alpha\Omega_K H^2}, \quad (6)$$

where D is the diffusion coefficient, Sc is the Schmidt number, and H is the density scale height. For this calculation, we use $\alpha = 10^{-3}$. By equating $t_{\text{stir}} = \xi t_{\text{sett}}$, we solve for the equilibrium height z_{sett} . The factor ξ is used to adjust the amount of settling for a grain size. $\xi = 1$ gives the settling height, z_{sett} , at which we expect to find the most grains of a particular size. The depletion height, z_{dep} , is found by setting $\xi = 100$ (Dullemond & Dominik 2004). Above this height, the abundance of dust grains of that size is almost entirely negligible.

We find that μm -sized grains in the inner ring would have settled between $z_{\text{sett}} = 10.5$ au and $z_{\text{dep}} = 16.0$ au by 3.5×10^5 yr. This is more consistent with the ring offset in the GPI data (Figure 3a) than the 18 au surface used by our model that does not consider vertical dust settling.

For the outer ring, we find that the μm -sized dust would have settled between $z_{\text{sett}} = 17.3$ au and $z_{\text{dep}} = 27.4$ au. This would give the outer ring surface a large enough z_{scat}/r fraction, where z_{scat} is the height of the scattering surface, to be illuminated in the GPI observation. However, the lack of the outer ring in the GPI observation (Figure 3a) implies that the outer ring may possess properties that result in an enhanced dust settling. This could be the result of shadowing if the outer ring’s micron-sized grains have settled deeper in its gas (Doi & Kataoka 2021). Guidi et al. (2022) found that there is not a significant difference in grain size between the inner and outer ring, which suggests that the enhanced scale height of the inner ring may be a result

of vertical mixing of dust from planets (Binkert et al. 2021).

We can artificially reduce the scale height of the outer ring compared to our fiducial model to determine the point at which it is no longer visible in scattered light. We find that vertically compressing the outer ring by just 5%, to 95% of the original scale height, and then recalculating the scattered light appearance is enough to decrease the brightness of the outer ring below the noise threshold of the GPI observation. Therefore, though we cannot determine the exact reduction in scale height, only a small change is necessary to match the observation.

7.2. DoAr 44: Inner Ring with Azimuthal Dimming

Our model correctly predicts that the surface brightness of the polarized scattered light from DoAr 44 is brightest inside of the 1.3 mm dust cavity. Our model does not show a local maximum in surface brightness within our radial domain unless the masking effect is taken into account. However, this peak in the model may simply occur at a radius that is smaller than we are able to explore due to our model limitations.

We find that the coronagraph used for the SPHERE observation will produce a local maximum around 15 au (Wahhaj et al. 2020). The difference between this 15 au in the model and the 20 au peak in the observation may be the result of a cavity in scattered light inside of the coronagraph edge. The lack of emission may be convolved with the beam and reduce the emission interior to 20 au, and thus move the peak from the coronagraph out to 20 au.

We are unable to run our model at smaller radii to investigate the scattered light further. The cavity of the disk causes the star light absorbing surface of the disk to meet the midplane of the disk around 15 au. Radially interior to this surface, the disk is optically thin to stellar radiation. One of the key assumptions of the radiative transfer code is the small angle approximation between the incoming stellar radiation and the absorbing surface. Another is that there is an optically thick region of the disk beneath the surface. Once the surface reaches the midplane, these assumptions are invalidated.

From both DoAr 44 and HD 163296, we find supporting evidence that the smaller fine dust does not have the same spatial distribution as the coarse dust. Dust settling in HD 163296 likely creates the non-detection of the second prominent fine dust ring with GPI. The scattered light model of DoAr 44 shows a slight bump around 47 au that is not present in the observation because the gas and dust follow the same distribution in the model. The difference between the model and data suggests that

the gas and fine dust distributions are smoother around 47 au than the mm-sized dust.

8. SUMMARY AND CONCLUSIONS

In this paper, we analyzed thermal emission and polarized scattered light images of the disks around HD 163296 and DoAr 44. These targets demonstrate the variety of ring-like substructures that may appear in disks. We used a radiative transfer code to find hydrostatic gas and mm-sized dust models that best fit the mm-sized dust observations. We used the conditions of these models in our consideration of plausible causes for their differing substructures and to help determine constraints on potential planets in the disks.

We found that Gaussian rings in our models are able to recreate the ringed substructures observed in thermal emission. Two distinct rings with small radial dispersions ($\sigma_r < 5$ au) recreate the rings of HD 163296. Conversely, the ring-skirt morphology of DoAr 44 is well modeled by three overlapping rings, two with larger radial dispersions ($\sigma_r \geq 9$ au) for the skirt and one with a tight radial dispersion for the ring ($\sigma_r = 2.8$ au). For this study, we focused on fitting the thermal emission data. The gas distributions of the disks appear to follow overall smoother distributions than the Gaussian rings we report.

We found notable differences between our models and the scattered light observations of HD 163296 and DoAr 44. For HD 163296, our model correctly predicted that the ring in polarized scattered light occurs at a smaller radius than the ring in thermal emission. However, the outer ring appears in our model but not the observation, which can be corrected by artificially reducing the scale height in the outer ring. For DoAr 44, our model replicated the peak in polarized scattered light that is found in the SPHERE observation to be within the coarse dust cavity. However, the lack of a ring at 47 au in the SPHERE observation compared to our model indicated that the gas and fine dust follow a smoother distribution than the coarse dust in our model. Furthermore, our assumptions for the model and the disk's cavity limit us to study the region beyond 15 au, so we cannot predict the scattered light from the inner disk.

We found a total dust masses of $81 \pm 13 M_\oplus$ and $82^{+26}_{-16} M_\oplus$ for the inner and outer ring of HD 163296 respectively. These estimates fall within the wide range of previous reports, but they are particularly close to the estimates from Rab et al. (2020), who fit models to both the $^{12}\text{CO } J = 2-1$ line and the 1.3 mm continuum. We found a total dust mass of $84^{+7.0}_{-3.5} M_\oplus$ for the disk around DoAr 44. This mass is roughly double the pre-

diction from Avenhaus et al. (2018), in which the dust mass was derived from blackbody emission assuming an optically thin disk with a constant temperature of 30 K. The discrepancy in our mass estimates is well explained by the differences in opacity and temperature between their model and ours.

Using gap opening criteria from Crida et al. (2006) and the pebble isolation mass, we calculated masses for planets that may be responsible for the gaps in the disk around HD 163296. The planet mass estimates depend on viscosity, but in the low-viscosity regime the mass limits are approximately $0.4\text{--}0.8 M_J$ and $0.9\text{--}2 M_J$ for the inner and outer gap respectively. The limits for the outer planet agree with the $1 M_J$ mass derived from deviations in the CO velocity channels (Izquierdo et al. 2021).

We found a lower limit of $0.5 M_J$ for the planet that may be responsible for the cavity of DoAr 44 based on the condition to open a gas cavity. Considering the possibility of a circumplanetary disk (CPD) being present, we calculated an upper mass limit of an optically thin CPD to be $3.5 M_{\oplus}$, assuming the same dust-to-gas ratio as the circumstellar disk. We derived an upper radius limit of an optically thick CPD to be 0.6 au. Using this radius as the disk truncation radius, we found an upper mass limit of $1.6 M_J$ for a planet in the case of an optically thick CPD.

An event like a giant impact may be able to explain the bright ring around DoAr 44 and the $\sim 1 M_{\oplus}$ dust excess on the north-west side of the disk. However, we also found that the bright ring in DoAr 44 may be a result of

radial drift of the coarse dust. Starting with a smooth gas distribution (Figure 17), we find that dust can accumulate into a bright ring in roughly 50,000 years (Figure 18). Though this explanation for the bright ring is favorably simpler compared to a giant impact, the short lifetimes of both phenomena would make observing either a lucky accident. This unlikely occurrence could be facilitated by our selection of DoAr 44 for its unusual and interesting structure from among dozens of possibilities.

We provided constraints for planets in these disks, but further observations of disks offer an avenue for improvements. Further analysis of disks at multiple wavelengths can help explain the apparent differences in the spatial distribution of various sized dust grains. More observations of gas emissions, like CO, from ALMA will help further characterization of the differences between the gas and large dust distributions in disks. Lastly, the advent of data from JWST will improve detection limits for planets in disks and help quantify the correlation between planets and disk substructures.

We would like to thank Henning Avenhaus and Sascha Quanz for providing their original VLT SPHERE images for use in our analysis. This work was supported by NASA XRP grant number 80NSSC20K0956. The work was conducted in part at the Jet Propulsion Laboratory, California Institute of Technology, under contract with the National Aeronautics and Space Administration.

REFERENCES

- ALMA Partnership, Brogan, C. L., Pérez, L. M., et al. 2015, *ApJL*, 808, L3, doi: [10.1088/2041-8205/808/1/L3](https://doi.org/10.1088/2041-8205/808/1/L3)
- Andrews, S. M., Huang, J., Pérez, L. M., et al. 2018, *ApJL*, 869, L41, doi: [10.3847/2041-8213/aaf741](https://doi.org/10.3847/2041-8213/aaf741)
- Avenhaus, H., Quanz, S. P., Garufi, A., et al. 2018, *ApJ*, 863, 44, doi: [10.3847/1538-4357/aab846](https://doi.org/10.3847/1538-4357/aab846)
- Avni, Y. 1976, *ApJ*, 210, 642, doi: [10.1086/154870](https://doi.org/10.1086/154870)
- Bae, J., Pinilla, P., & Birnstiel, T. 2018, *ApJL*, 864, L26, doi: [10.3847/2041-8213/aadd51](https://doi.org/10.3847/2041-8213/aadd51)
- Bae, J., Teague, R., Andrews, S. M., et al. 2022, *ApJL*, 934, L20, doi: [10.3847/2041-8213/ac7fa3](https://doi.org/10.3847/2041-8213/ac7fa3)
- Baruteau, C., Crida, A., Paardekooper, S. J., et al. 2014, in *Protostars and Planets VI*, ed. H. Beuther, R. S. Klessen, C. P. Dullemond, & T. Henning, 667, doi: [10.2458/azu_uapress.9780816531240-ch029](https://doi.org/10.2458/azu_uapress.9780816531240-ch029)
- Binkert, F., Szulágyi, J., & Birnstiel, T. 2021, *MNRAS*, 506, 5969, doi: [10.1093/mnras/stab2075](https://doi.org/10.1093/mnras/stab2075)
- Birnstiel, T., Klahr, H., & Ercolano, B. 2012, *A&A*, 539, A148, doi: [10.1051/0004-6361/201118136](https://doi.org/10.1051/0004-6361/201118136)
- Birnstiel, T., Dullemond, C. P., Zhu, Z., et al. 2018, *ApJL*, 869, L45, doi: [10.3847/2041-8213/aaf743](https://doi.org/10.3847/2041-8213/aaf743)
- Blum, J., & Wurm, G. 2008, *ARA&A*, 46, 21, doi: [10.1146/annurev.astro.46.060407.145152](https://doi.org/10.1146/annurev.astro.46.060407.145152)
- Brunngräber, R., & Wolf, S. 2019, *A&A*, 627, L10, doi: [10.1051/0004-6361/201935169](https://doi.org/10.1051/0004-6361/201935169)
- Calvet, N., Patino, A., Magris, G. C., & D’Alessio, P. 1991, *ApJ*, 380, 617, doi: [10.1086/170618](https://doi.org/10.1086/170618)
- Casassus, S., Avenhaus, H., Pérez, S., et al. 2018, *MNRAS*, 477, 5104, doi: [10.1093/mnras/sty894](https://doi.org/10.1093/mnras/sty894)
- Chiang, E. I., & Goldreich, P. 1997, *ApJ*, 490, 368, doi: [10.1086/304869](https://doi.org/10.1086/304869)
- Cieza, L. A., González-Ruilova, C., Hales, A. S., et al. 2021, *MNRAS*, 501, 2934, doi: [10.1093/mnras/staa3787](https://doi.org/10.1093/mnras/staa3787)

- Crida, A., Morbidelli, A., & Masset, F. 2006, *Icarus*, 181, 587, doi: [10.1016/j.icarus.2005.10.007](https://doi.org/10.1016/j.icarus.2005.10.007)
- D'Alessio, P., Calvet, N., & Hartmann, L. 2001, *ApJ*, 553, 321, doi: [10.1086/320655](https://doi.org/10.1086/320655)
- D'Alessio, P., Cantö, J., Calvet, N., & Lizano, S. 1998, *ApJ*, 500, 411, doi: [10.1086/305702](https://doi.org/10.1086/305702)
- Doi, K., & Kataoka, A. 2021, arXiv e-prints, arXiv:2102.06209. <https://arxiv.org/abs/2102.06209>
- Duffell, P. C. 2020, *ApJ*, 889, 16, doi: [10.3847/1538-4357/ab5b0f](https://doi.org/10.3847/1538-4357/ab5b0f)
- Dullemond, C. P., & Dominik, C. 2004, *A&A*, 421, 1075, doi: [10.1051/0004-6361:20040284](https://doi.org/10.1051/0004-6361:20040284)
- Dullemond, C. P., Juhasz, A., Pohl, A., et al. 2012, RADMC-3D: A multi-purpose radiative transfer tool. <http://ascl.net/1202.015>
- Dullemond, C. P., Birnstiel, T., Huang, J., et al. 2018, *ApJL*, 869, L46, doi: [10.3847/2041-8213/aaf742](https://doi.org/10.3847/2041-8213/aaf742)
- Fairlamb, J. R., Oudmaijer, R. D., Mendigutía, I., Ilee, J. D., & van den Ancker, M. E. 2015, *MNRAS*, 453, 976, doi: [10.1093/mnras/stv1576](https://doi.org/10.1093/mnras/stv1576)
- Flock, M., Dzyurkevich, N., Klahr, H., Turner, N. J., & Henning, T. 2011, *ApJ*, 735, 122, doi: [10.1088/0004-637X/735/2/122](https://doi.org/10.1088/0004-637X/735/2/122)
- Foreman-Mackey, D., Hogg, D. W., Lang, D., & Goodman, J. 2013, *PASP*, 125, 306, doi: [10.1086/670067](https://doi.org/10.1086/670067)
- Gaia Collaboration, Brown, A. G. A., Vallenari, A., et al. 2018, *A&A*, 616, A1, doi: [10.1051/0004-6361/201833051](https://doi.org/10.1051/0004-6361/201833051)
- Gonzalez, J. F., Laibe, G., & Maddison, S. T. 2017, *MNRAS*, 467, 1984, doi: [10.1093/mnras/stx016](https://doi.org/10.1093/mnras/stx016)
- Guidi, G., Isella, A., Testi, L., et al. 2022, *A&A*, 664, A137, doi: [10.1051/0004-6361/202142303](https://doi.org/10.1051/0004-6361/202142303)
- Guilera, O. M., Cuello, N., Montesinos, M., et al. 2019, *MNRAS*, 486, 5690, doi: [10.1093/mnras/stz1158](https://doi.org/10.1093/mnras/stz1158)
- Gundlach, B., Kiliyas, S., Beitz, E., & Blum, J. 2011, *Icarus*, 214, 717, doi: [10.1016/j.icarus.2011.05.005](https://doi.org/10.1016/j.icarus.2011.05.005)
- Hartmann, L., Calvet, N., Gullbring, E., & D'Alessio, P. 1998, *ApJ*, 495, 385, doi: [10.1086/305277](https://doi.org/10.1086/305277)
- Heinemann, T., & Papaloizou, J. C. B. 2009, *MNRAS*, 397, 52, doi: [10.1111/j.1365-2966.2009.14799.x](https://doi.org/10.1111/j.1365-2966.2009.14799.x)
- Henyey, L. G., & Greenstein, J. L. 1941, *ApJ*, 93, 70, doi: [10.1086/144246](https://doi.org/10.1086/144246)
- Isella, A., Guidi, G., Testi, L., et al. 2016, *PhRvL*, 117, 251101, doi: [10.1103/PhysRevLett.117.251101](https://doi.org/10.1103/PhysRevLett.117.251101)
- Isella, A., Huang, J., Andrews, S. M., et al. 2018, *ApJL*, 869, L49, doi: [10.3847/2041-8213/aaf747](https://doi.org/10.3847/2041-8213/aaf747)
- Izquierdo, A. F., Facchini, S., Rosotti, G. P., van Dishoeck, E. F., & Testi, L. 2021, arXiv e-prints, arXiv:2111.06367. <https://arxiv.org/abs/2111.06367>
- Jang-Condell, H. 2008, *ApJ*, 679, 797, doi: [10.1086/533583](https://doi.org/10.1086/533583)
- . 2009, *ApJ*, 700, 820, doi: [10.1088/0004-637X/700/1/820](https://doi.org/10.1088/0004-637X/700/1/820)
- Jang-Condell, H., & Sasselov, D. D. 2003, *ApJ*, 593, 1116, doi: [10.1086/376569](https://doi.org/10.1086/376569)
- Kenyon, S. J., & Hartmann, L. 1987, *ApJ*, 323, 714, doi: [10.1086/165866](https://doi.org/10.1086/165866)
- Keppler, M., Benisty, M., Müller, A., et al. 2018, *A&A*, 617, A44, doi: [10.1051/0004-6361/201832957](https://doi.org/10.1051/0004-6361/201832957)
- Lambrechts, M., Johansen, A., & Morbidelli, A. 2014, *A&A*, 572, A35, doi: [10.1051/0004-6361/201423814](https://doi.org/10.1051/0004-6361/201423814)
- Leinhardt, Z. M., & Stewart, S. T. 2012, *ApJ*, 745, 79, doi: [10.1088/0004-637X/745/1/79](https://doi.org/10.1088/0004-637X/745/1/79)
- Monnier, J. D., Harries, T. J., Aarnio, A., et al. 2017, *ApJ*, 838, 20, doi: [10.3847/1538-4357/aa6248](https://doi.org/10.3847/1538-4357/aa6248)
- Muro-Arena, G. A., Dominik, C., Waters, L. B. F. M., et al. 2018, *A&A*, 614, A24, doi: [10.1051/0004-6361/201732299](https://doi.org/10.1051/0004-6361/201732299)
- Pineda, J. E., Szulágyi, J., Quanz, S. P., et al. 2019, *ApJ*, 871, 48, doi: [10.3847/1538-4357/aaf389](https://doi.org/10.3847/1538-4357/aaf389)
- Pinte, C., Price, D. J., Ménard, F., et al. 2018, *ApJL*, 860, L13, doi: [10.3847/2041-8213/aac6dc](https://doi.org/10.3847/2041-8213/aac6dc)
- Pringle, J. E. 1981, *ARA&A*, 19, 137, doi: [10.1146/annurev.aa.19.090181.001033](https://doi.org/10.1146/annurev.aa.19.090181.001033)
- Rab, C., Kamp, I., Dominik, C., et al. 2020, *A&A*, 642, A165, doi: [10.1051/0004-6361/202038712](https://doi.org/10.1051/0004-6361/202038712)
- Ricci, L., Testi, L., Natta, A., & Brooks, K. J. 2010, *A&A*, 521, A66, doi: [10.1051/0004-6361/201015039](https://doi.org/10.1051/0004-6361/201015039)
- Rosotti, G. P., Juhasz, A., Booth, R. A., & Clarke, C. J. 2016, *MNRAS*, 459, 2790, doi: [10.1093/mnras/stw691](https://doi.org/10.1093/mnras/stw691)
- Sallum, S., Follette, K. B., Eisner, J. A., et al. 2015, *Nature*, 527, 342, doi: [10.1038/nature15761](https://doi.org/10.1038/nature15761)
- Shakura, N. I., Sunyaev, R. A., & Zilitinkevich, S. S. 1978, *A&A*, 62, 179
- Stammler, S. M., Birnstiel, T., Panić, O., Dullemond, C. P., & Dominik, C. 2017, *A&A*, 600, A140, doi: [10.1051/0004-6361/201629041](https://doi.org/10.1051/0004-6361/201629041)
- van der Marel, N., Dong, R., di Francesco, J., Williams, J. P., & Tobin, J. 2019, *ApJ*, 872, 112, doi: [10.3847/1538-4357/aafd31](https://doi.org/10.3847/1538-4357/aafd31)
- van der Marel, N., van Dishoeck, E. F., Bruderer, S., et al. 2016, *A&A*, 585, A58, doi: [10.1051/0004-6361/201526988](https://doi.org/10.1051/0004-6361/201526988)
- Wahhaj, Z., Milli, J., Rodler, F., et al. 2020, Very Large Telescope: SPHERE User Manual, ESO
- Zhang, K., Blake, G. A., & Bergin, E. A. 2015, *ApJL*, 806, L7, doi: [10.1088/2041-8205/806/1/L7](https://doi.org/10.1088/2041-8205/806/1/L7)
- Zhou, Y., Sanghi, A., Bowler, B. P., et al. 2022, *ApJL*, 934, L13, doi: [10.3847/2041-8213/ac7fef](https://doi.org/10.3847/2041-8213/ac7fef)